Electronic Supplementary Information

Platinum nanoparticles partially-embedded into carbon sphere surface: a low metal-loading anode catalyst with superior performance for direct methanol fuel cells

Kui Li,[abc] Zhao Jin,[ac] Junjie Ge,*[ac] Changpeng Liu*[ac] and Wei Xing*[acd]

Corresponding author: Changpeng Liu, E-mail: liuchp@ciac.ac.cn

Tel.: 86-431-85262225; Fax: 86-431-85262225

* Corresponding author: Junjie Ge, E-mail: gejj@ciac.ac.cn

Tel.: 86-431-85262225; Fax: 86-431-85262225

* Corresponding author: Wei Xing, E-mail: xingwei@ciac.ac.cn

Tel.: 86-431-85262223; Fax: 86-431-85262225

[a] *Laboratory of Advanced Power Sources, Changchun Institute of Applied Chemistry, Chinese Academy of Sciences, Changchun, Jilin, 130022, PR China*

[b] *University of Chinese Academy of Sciences, Beijing, 100039, PR China*

[c] *Jilin Province Key Laboratory of Low Carbon Chemical Power Sources, Changchun, Jilin, 130022, PR China*

[d] *State Key Laboratory of Electroanalytical Chemistry, Changchun Institute of Applied Chemistry, Chinese Academy of Sciences, Changchun, Jilin, 130022, PR China*

Experimental section:

1 Synthesis of Pt nanoparticles embedded on resorcinol-formaldehyde resin carbon (Pt@RFC) catalyst.

The Pt@RFC was synthesized by heating mixtures of resorcinol-formaldehyde resin (a carbon precursor) and chloroplatinic acid (H_2PtCl_6). The preparation process of the support materials was similar with our former works and the preparation method of RFC could be also obtained from that.[1] We should emphasized that the reaction time is constant (twenty four hours). In a typical process, a mixture containing certain amount of ammonium, as the catalyst, and 400 mg resorcinol were dispersed in 50 mL distilled deionized water, magnetically stirring for 30 min. Then the solution was heated at 94°C while 0.560 mL aqueous formaldehyde solution was added and stirred under reflux, which time is set as the starting time. After t_{add} (t_{add} =1, 4, 8, 12, 20 hours) later, we added the H_2PtCl_6 as the Pt source during the reaction. Twenty four hours later, the suspension was vacuum-dried at room temperature and milled to obtain an $[PtCl_6]^{2-}$@resorcinol-formaldehyde resin powder, and then programmed calcined at 400°C for Pt reduction and 900°C for RFC carbonization in an Ar-H_2 (10%) gas atmosphere. Afterward, the Pt@RFC-t_{add} was obtained after being ground into a powder and washed with deionized water.

2 Synthesis of the Pt based catalysts deposited on supports materials.

Pt/RFC catalysts with a Pt loading of 20 wt. % were synthesized through a process with ethylene glycol (EG) as the reducing agent. Firstly, 20 mg of RFC was suspended in 20 ml of an ethylene glycol solution, and a 332 μL H_2PtCl_6 solution (15.067 mg $_{Pt}$ mL^{-1}) was added. Then, the mixture was heated at 150°C for 3 h. Subsequently, the suspension was filtered and washed with deionized water and then dried at 80°C for 10 h to obtain the Pt/RFC catalysts.

3 Physical characterizations

Transmission electron microscopy (TEM), high-resolution transmission electron microscopy (HRTEM) and high-angle annular dark-field scanning transmission electron microscopy (STEM) were conducted on a on a Philips TECNAI G2 electron microscope operated at 200 kV.

Energy dispersive X-ray analysis (EDX) and element mapping analysis were conducted on a XL30 ESEM FEG field emission scanning electron microscope (SEM) operating at 20 kV.

X-Ray photoelectron spectroscopy (XPS) measurements were carried out on a Kratos XSAM-800 spectrometer with an Mg Kα radiation source.

X-Ray diffraction (XRD) measurements were performed with a PW1700 diffract meter (Philips Co.) using a Cu Kα (λ=0.15405 nm) radiation source. The obtained XRD patterns were analyzed with Jade 5.0 software to remove the background radiation.

The textural and morphological features of the different carbon supports and catalysts prepared were determined by means of nitrogen physisorption at 77 K in a Quantachrome Autosorb-iQ. Textural properties such as specific surface area, pore volume, and pore size distribution were calculated from each corresponding nitrogen adsorption-desorption isotherm applying the Brunauer-Emmet-Teller (BET) equation and Barrett-Joyner-Halenda (BJH) and t-plot methods in ASiQwin 3.01 program.

All elemental analyses of catalyst samples were analyzed by ICP-AES-MS (Inductivity Coupled Plasma-Atomic Emission Spectroscopy-Mass Spectroscopy) on a Thermo Elemental IRIS Intrepid.

Thermo-gravimetric analysis was performed on a thermogravimetric analyzer (TGA Q-50) over a temperature range of 50~900°C at a heating rate of 10°C min^{-1}.

4 Electrochemical measurements

Electrochemical measurements were carried out with an EG & G PARSTAT 4000 potentiostat/galvanostat (Princeton Applied Research Co., USA) in a conventional three electrode test cell. The catalyst ink was prepared by ultrasonically dispersing a mixture containing 5 mg of catalyst, 950 μL of ethanol and 50 μL of 5wt % Nafion solution. Next, 5 μL of the catalyst ink was pipetted onto a pre-cleaned glassy carbon disk (diameter = 4 mm) (polish with 0.3 and 0.05 mm alumina powder, sonicated and rinsed with deionized water) as the working electrode. A Pt foil and a saturated calomel electrode (SCE) were used as the counter and the reference electrodes, respectively. All of the potentials are relative to the SCE electrode, unless otherwise noted. In order to activate and clean the catalyst surface, the working electrodes were potentially cycled from -0.2 V and 1.0 V at a scan rate of 50 mV s^{-1} in 0.5 M H$_2$SO$_4$ solution until a stable response was obtained. (About 50 cycles) To evaluate the activity of the catalysts for methanol oxidation reaction (MOR), cyclic voltammograms (CVs) measurements were performed at room temperature between -0.2V and 1.0 V in an electrolyte solution containing 1.0 M CH$_3$OH and 0.5 M H$_2$SO$_4$, with scan rates of 50 mV s^{-1}. To investigate the anti-posing ability of the catalysts, 99.99% pure CO was purged to the cells filled with 0.5 M H$_2$SO$_4$ electrolyte for 30 min while the working electrode was held at 0.02 V vs. SCE. N$_2$ was then purged to the system for 30 min to remove non-adsorbed CO before the measurements were made. The CO stripping was performed in the potential range of -0.2~1.0 V at a scan rate of 50 mV s^{-1}. The electrochemical active surface areas (ECSA) and the tolerance to CO poisoning were estimated by the CO stripping test, assuming that the Coulombic charge required for the oxidation of the CO monolayer was 420 μC cm^{-2}. To estimate the stability of the catalysts, the chronoamperometric (CA) experiments were performed in still 0.5 M H$_2$SO$_4$ and 1 M CH$_3$OH solutions at 0.5 V. The electrochemical impedance spectra (EIS) were recorded at 10 points per decade over the frequency range from 100 kHz to 10 mHz. The amplitude of the sinusoidal potential signal was 5

4

mV. All electrolyte solutions were de-aerated by high-purity nitrogen for at least 20 min prior to each measurement.

5 MEA Fabrication and Single-cell Performance Test.

Nafion 117 (DuPont) was used as the proton exchange membranes and the pre-treatment of the Nafion membrane was accomplished by successively treating the membrane in 5 wt. % H_2O_2 solution at 80℃, distilled water at 80°C, 8 wt.% H_2SO_4 solution at 80°C and then in distilled water at 80°C again, for 30 min in each step.

Membrane electrode assemblies (MEAs) with a 25 cm^2 active cell area were fabricated using a 'direct paint' technique to apply the catalyst layer. The 'catalyst inks' were prepared by dispersing the catalyst nanoparticles into appropriate amounts of Millipore® water and a 5% recast Nafion® solution. Anode and cathode 'catalyst inks' were directly painted onto carbon paper (TGPH060, 20 wt. % PTFE, Toray). For all MEAs in this study, the cathode consisted of commercial Pt/C (60 wt. %, Johnson Matthey) at a standard metal loading of 2 mg cm^{-2}. The anode consisted of carbon supported commercial PtRu/C (20 wt. % Pt and 10 wt. % Ru, Johnson Matthey) and Pt@RFC catalysts. A single cell test fixture consisted of machined graphite flow fields with direct liquid feeds and gold plated copper plates to avoid corrosion (Fuel Cell Technologies Inc.). Hot-pressing was conducted at 135°C and 6 atm for 90 s.

The MEA was fitted between two graphite plates in a punctual flow bed. The polarization curves were obtained using a Fuel Cell Test System (Arbin Instrument Corp.) under the operation conditions of 40, 60 and 80°C. High purity O_2 (99.99 %) is applied as the oxidant at 1.0 L min^{-1} as the cathode atmosphere and 1 M methanol as the reactant feed at the anode side at 13.5 mL min^{-1}. The potential range is from the open circuit potential to 0.05V, and one point is collected every 0.05 mA where a delay of 1 minute was applied to get the

steady state plots. Both sides are under ambient pressure. Discharge curves was operation at 0.3 V (60°C) for

12 hours for all fuel cells.

The synthesis process for Pt@RFC is illustrated in **Fig. 1a**. Firstly, a gold yellow solution is obtained by adding ammonia, which is divorced the proton from phenolic hydroxyl in addition reaction. Then mixing with formaldehyde, the reactants polymerize to milky emulsion. With the extent of polymerization increased the colloid turns yellow as adding the H_2PtCl_6, which further catalyzes the condensation reaction and is in coordination with $-CH_2^+$. The immobilized $[PtCl_6]^{2-}$ ions are then reduced into metallic state by the isolated formaldehyde in the reaction system.[2, 3] The XPS was used to further detect surface Pt state. As shown in **Fig. S1a**, the major component in the Pt 4f was metallic Pt (0). Moreover, the presence of little Pt (II) may derive from the surface oxidation of the Pt nanoparticles at RF gel. After carbonization under reducing atmosphere, the metal particles are confined and some surface amorphous carbon is swept out.[4, 5] Thus, the earlier adding-time for H_2PtCl_6, the more inner position for Pt nanoparticles.

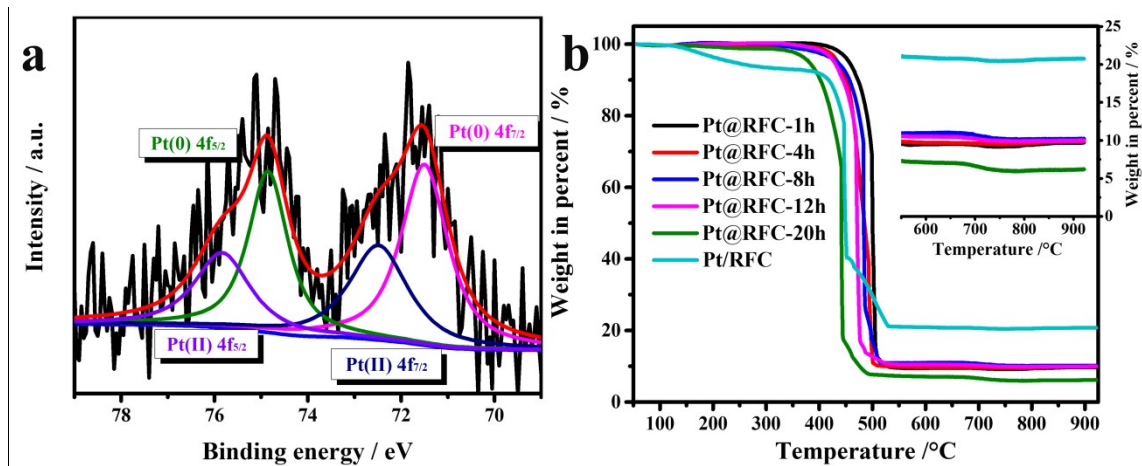**Fig. S1** (a) XPS patterns of Pt@RFR for Pt 4f5/2 and Pt 4f7/2 binding energy; (b) The TGA curves of Pt@RFC and Pt/RFC catalysts. The inset shows the final PtO_2 content of these catalysts range from 550 to 900ºC with enlarge scale.

Table S1 The mass fraction of Pt in all catalysts obtained from TGA curves and ICP-AES-MS measurement.

Catalysts	Calculations from TGA in percent* (%)	ICP results** (ppm)	Calculations from ICP-AES in percent (%)
Pt/C-JM	-	1982	19.82
Pt/RFC	20.76	2023	20.23
Pt@RFC-1h	9.71	215	2.15
Pt@RFC-4h	9.88	531	5.31
Pt@RFC-8h	10.20	883	8.83
Pt@RFC-12h	10.00	957	9.57
Pt@RFC-20h	6.20	612	6.12

* The Pt weight percent was converted from the final value in TGA based on PtO_2.

** Here, the volume of sample is 10 mL, which was filtrated from washing the as-synthesized catalysts (100 mg) with the aqua regia (10 mL).

Filtrates from product solution
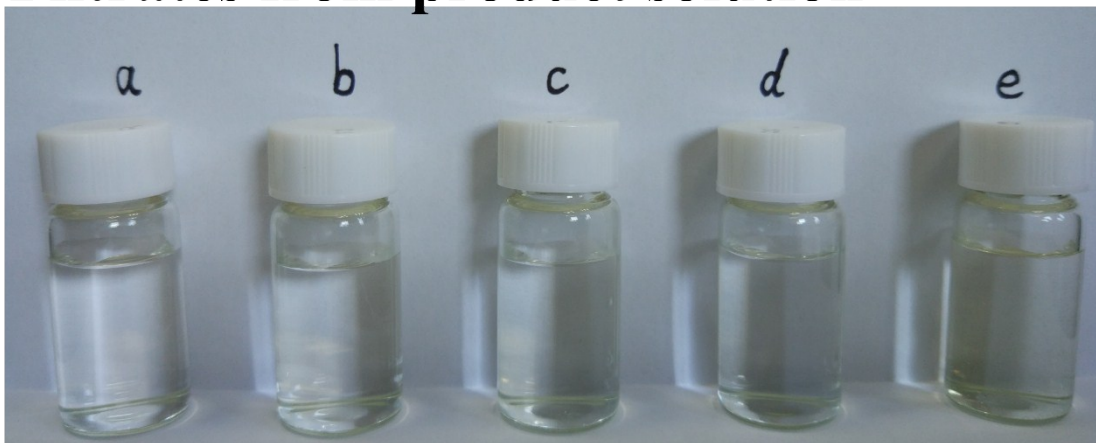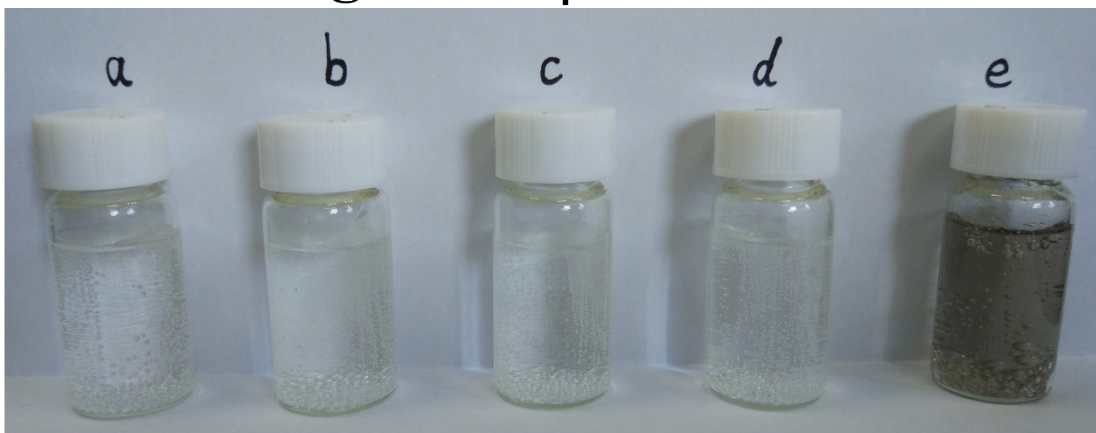

After adding NaBH₄

Fig. S2 The upper photo shows the filtrates from the product solution and the below one records color change of the liquid after adding NaBH$_4$. The symbol a, b, c, d and e represents the Pt@RFC-1h, 4h, 8h, 12h and 20h, respectively.

The synthesis of the Pt@RFC-8h catalyst is carefully observed by SEM (**Fig. S3**) to confirm that all Pt nanoparticles are uniformly confined in the mesoporous carbon sphere. In **Fig. S3a**, the isolated carbon spheres ca. 460 nm are observed, with an amount of metal particles located on the external carbon surface (the white points). Considering that the Pt@RFC-8h catalyst in **Fig. S3b** thermally treated at 900°C for the carbonization of impregnated polymers, the carbon sphere is in mono-dispersion with a uniform size about 340 nm, resulting Pt NPs are thus in-situ confined in the nonporous of resorcinol-formaldehyde carbon, rather than situating at the external boundary of the carbon shells.
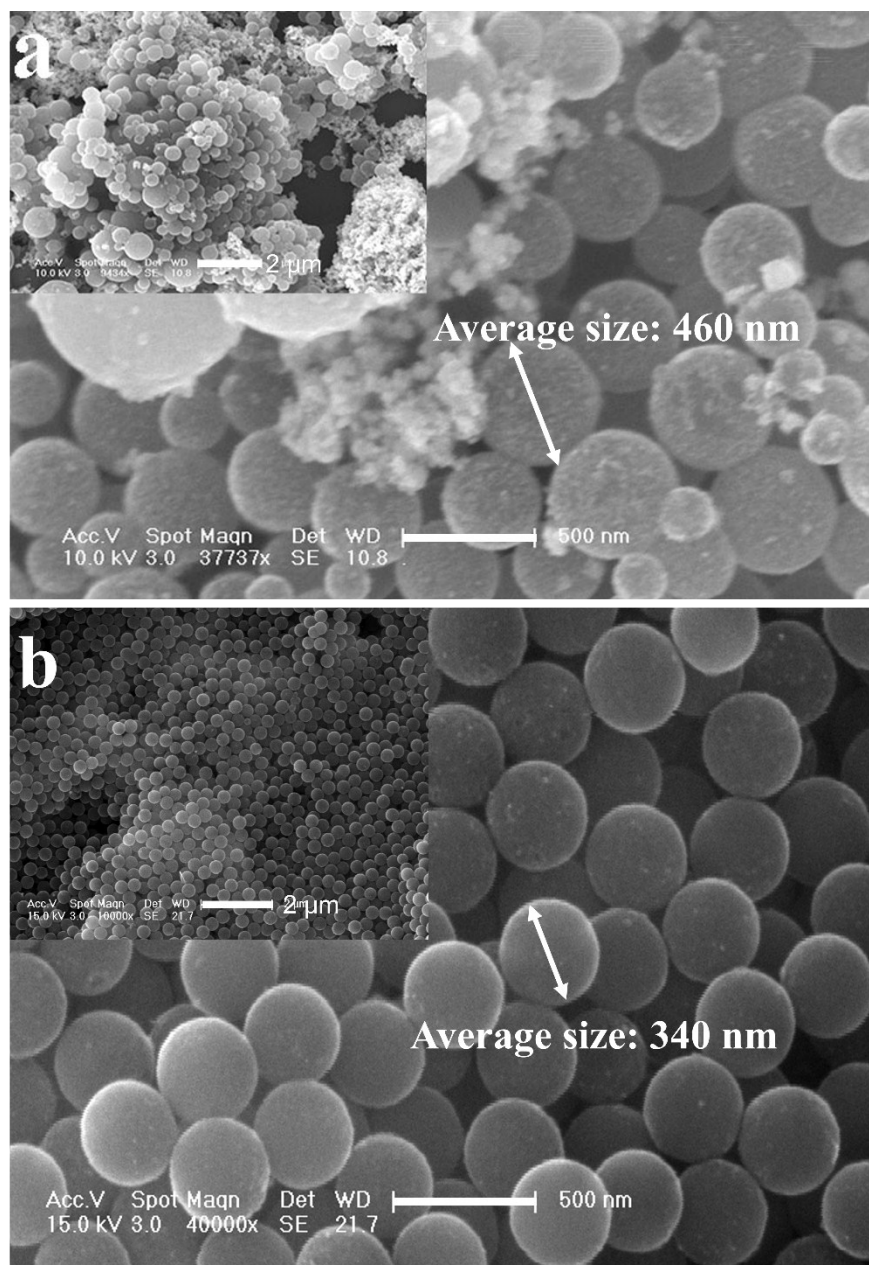
Fig. S3 SEM images of (a) Pt/RFC and (b) Pt@RFC-8h catalysts; the inset shows the morphology of the catalysts in large scale bar.
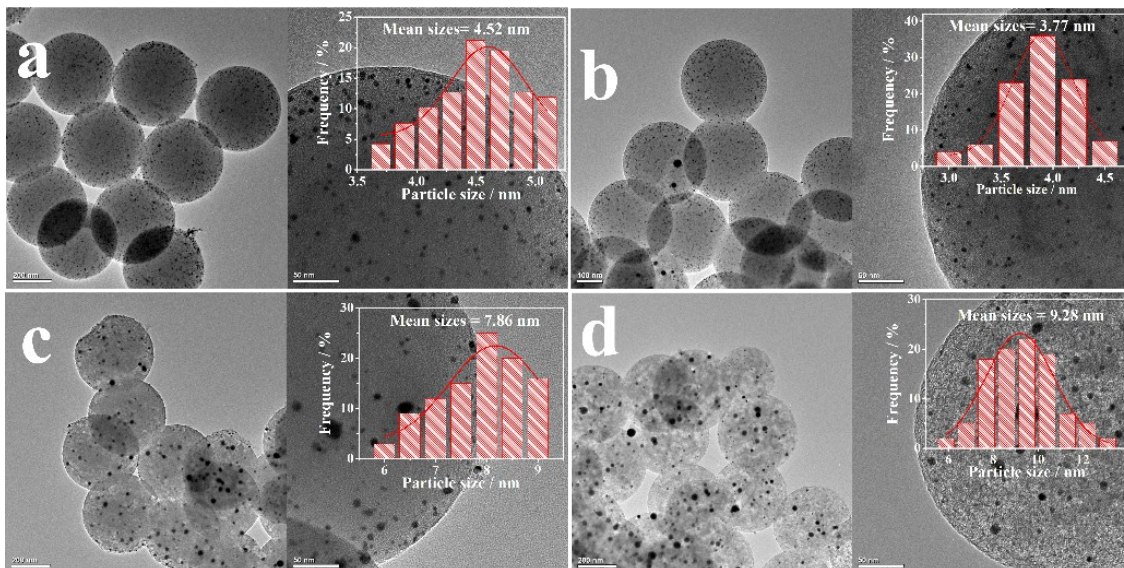
Fig. S4 TEM images and the corresponding particle size distribution histograms of Pt@RFC catalysts: a, b, c and d represents the Pt@RFC-1h, 4h, 12h and 20h, respectively.
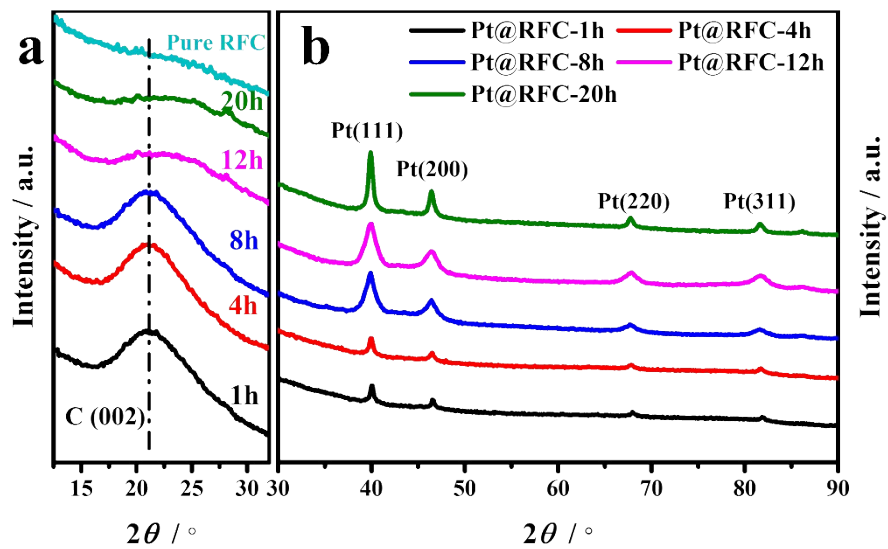
Fig. S5 The peak of C (002) (a) and Pt (b) for the as-prepared Pt@RFC catalysts.

Table S2 Particle size of Pt@RFC, Pt/RFC and Pt/C-JM catalysts obtained by TEM and XRD measurements.

Catalysts	Particles size (nm)	
	By TEM	By XRD
Pt/C-JM	2.84	2.56
Pt/RFC	3.04	3.36
Pt@RFC-1h	4.52	4.76
Pt@RFC-4h	3.77	3.43
Pt@RFC-8h	2.03	2.31
Pt@RFC-12h	7.86	6.83
Pt@RFC-20h	9.28	10.01
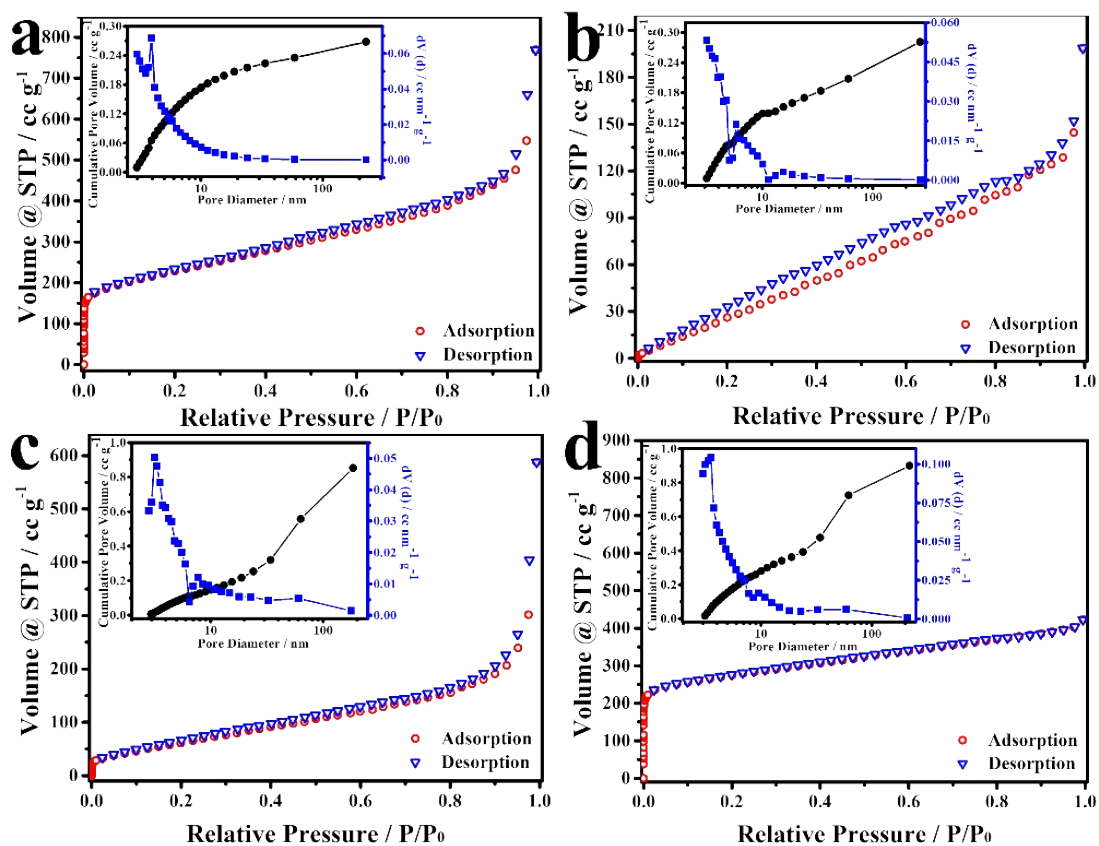
Fig. S6 Typical nitrogen adsorption-desorption isotherm and BJH pore size distribution plots (inset) of (a) Pt@RFC-8h; (b) Pt/RFC; (c) Pt/C-JM; and (d) Pure RFC.

Table S3 BET surfaces area, BJH desorption average pore size and pore volume of Pt@RFC-8h, Pt/RFC, Pt/C-JM catalysts and pure RFC.

Catalysts	BET surfaces area ($m^2 g^{-1}$)	Average pore size (nm)	Pore Volume (cc g^{-1})
Pt@RFC-8h	805.9	3.93	1.190
Pt/RFC	192.9	3.14	0.307
Pt/C-JM	263.2	3.32	0.909
Pure RFC	1018.8	3.12	0.654

Table S4 Binding energies of the Pt $4f_{7/2}$ components and the O/C ratio for the Pt@RFC-8h, Pt/RFC and Pt/C-JM catalysts.

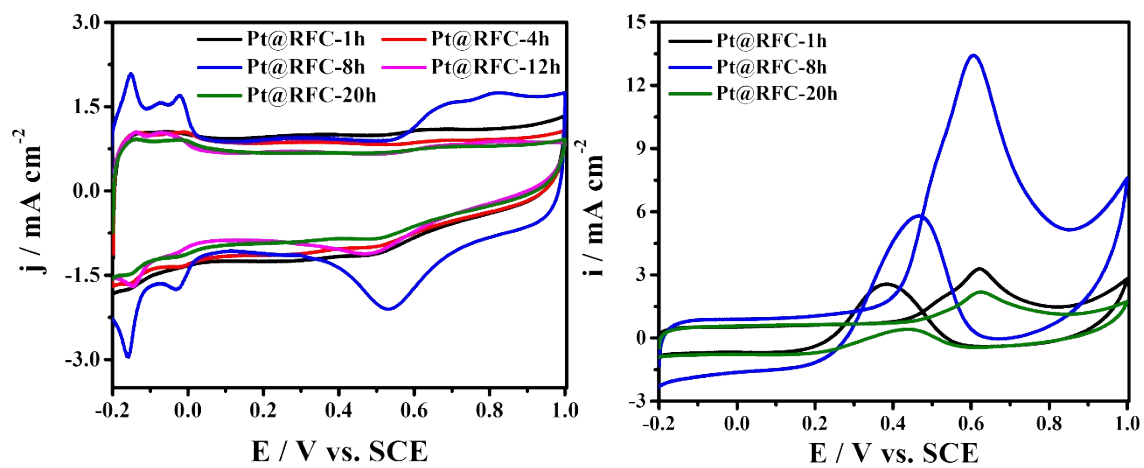| Catalysts	Assignment	Binding energy (eV)	Relative intensity (%)	O/C ratio (%)
Pt@RFC-8h	Pt(0)	71.01	79.5	1.89
	Pt(II)-Pt(OH)$_2$	72.06	20.5	
Pt/RFC	Pt(0)	71.28	61.4	6.92
	Pt(II)-Pt(OH)$_2$	72.03	38.6	
Pt/C-JM	Pt(0)	71.45	65.2	5.57
	Pt(II)-Pt(OH)$_2$	72.28	34.8	

Fig. S7 CVs of the Pt@RFC catalysts in 0.5 M H_2SO_4 with a scanning rate of 50 mV s^{-1}. The curves were

normalized in the area of glass carbon electrode (0.1257 cm^2) and the catalysts loading is 0.2 mg cm^{-2}.

Table S5 Electrochemical surface area (ECSA) estimation from CO stripping experiment and CV in 0.5 M H$_2$SO$_4$ with a scanning rate of 50 mV s^{-1}. The onset and peak potential for CO stripping for the different Pt-based catalysts in 0.5 M H$_2$SO$_4$ with a scanning rate of 50 mV s^{-1}. The area of glass carbon electrode is 0.1257 cm^2 and the catalysts loading is 0.2 mg cm^{-2}.

Catalysts	S$_H$ (cm^2)	ECSA$_H$ (m^2 g^{-1})	S$_{CO}$ (cm^2)	ECSA$_{CO}$ (m^2 g^{-1})	Onset Potential (mV)	Peak potential (mV)
Pt/C-JM	3.19	63.8	3.22	64.4	555.2	625.4
Pt/RFC	2.66	53.2	2.73	54.6	433.9	518.0
Pt@RFC-1h	0.31	12.4	-	-	-	-
Pt@RFC-4h	0.59	23.4	-	-	-	-
Pt@RFC-8h	2.02	80.8	1.96	79.4	402.3	478.2
Pt@RFC-12h	0.96	38.5	-	-	-	-
Pt@RFC-20h	0.57	37.8	-	-	-	-

Table S6 Comparison of mass activity between the novel Pt@RFC-8h catalyst and other Pt-based catalysts reported in the literature.

Sample	Electrolyte	Scan rate (mV s^{-1})	Scan scope	Mass activity (mA mg$_{Pt}^{-1}$)	Ref.
Pt@RFC-8h	1.0 M CH$_3$OH + 0.5 M H$_2$SO$_4$	50	-0.2~1.0 V *vs.* SCE	657.4	This work
Pt-RGO/PF-x	1.0 M CH$_3$OH + 0.5 M H$_2$SO$_4$	50	-0.2~1.0 V *vs.* SCE	404	[6]
Pt/C$_{Ru-dim}$	0.5 M CH$_3$OH + 0.5 M H$_2$SO$_4$	20	0.05~1.2 V *vs.* SHE	344.3	[7]
Pt/CeO$_2$/PANI THNRAs	0.5 M CH$_3$OH + 0.5 M H$_2$SO$_4$	100	-0.2~1.0 V *vs.* SCE	360	[8]
Pt-Co-P-11.9/CNT,	1.0 M CH$_3$OH + 0.5 M H$_2$SO$_4$	50	-0.2~1.0 V *vs.* SCE	535.3	[9]
Pt/TiO$_2$-C	1.0 M CH$_3$OH + 0.5 M H$_2$SO$_4$	50	-0.204~0.991 V *vs.* Ag/AgCl	415	[10]
Pt/Graphene-350	1.0 M CH$_3$OH + 0.5 M H$_2$SO$_4$	50	-0.05~1.0 V *vs.* SCE	180.74	[11]
Pt/TiC NWs	1.0 M CH$_3$OH + 0.1 M H$_2$SO$_4$	20	0~1.0 V *vs.* SCE	350	[12]
Pt/TiO$_2$@NC$_x$-900	1.0 M CH$_3$OH + 0.5 M H$_2$SO$_4$	50	-0.242~0.958 V *vs.* SCE	354.75	[13]
Pt/HO-CNTs	1.0 M CH$_3$OH + 0.5 M H$_2$SO$_4$	50	-0.2~0.948 V *vs.* SCE	590	[14]
Pt/CPF-C	0.5 M CH$_3$OH + 0.5 M H$_2$SO$_4$	50	0~0.8 V *vs.* Ag/AgCl	443	[15]
Pt/W$_{18}$O$_{49}$	0.5 M CH$_3$OH + 0.5 M H$_2$SO$_4$	50	-0.242~0.958 V *vs.* SCE	422.37	[16]
Pt/p-H$_x$MoO$_3$	1.0 M CH$_3$OH + 0.5 M H$_2$SO$_4$	50	-0.2~1.2 V *vs.* Ag/AgCl	100.5	[17]
Pt/Ti$_{0.8}$Mo$_{0.2}$N	1.0 M CH$_3$OH + 0.5 M H$_2$SO$_4$	50	-0.2~1.0 V *vs.* Ag/AgCl	611	[18]

Table S7 Electrocatalytic performance and CA results for the comparison catalysts in 1.0 M CH_3OH and 0.5 M H_2SO_4 solution.

Catalysts	Specific activity (mA cm^{-2})	Mass activity (mA mg $_{Pt}$$^{-1}$)	Onset potential (mV)	Peak potential (mV)	After CA test for 7200s	
					Mass activity (mA mg $_{Pt}$$^{-1}$)	Decline in percent (%)
Pt@RFC-8h	0.838	657.4	359.1	606.9	559.3	13.6
Pt/RFC	0.536	292.8	430.2	644.7	26.9	90.8
Pt/C-JM	0.535	344.5	441.7	634.5	114.4	66.8

The CVs at the Pt@RFC, Pt/RFC and Pt/C-JM electrodes in 0.5 M H_2SO_4 solutions containing 1.0 M CH_3OH solution are also shown in **Fig. S8** with different scan rates of 2, 5, 10, 20, 50, 75 and 100 mV s^{-1}. The curves of the peak current *vs.* the square root of scan rates are inserted in the corresponding **Fig. S8**. The peak current is increasing with improving the scan rate. The linear relationship is attributed to a diffusion controlled process. The relationship between the current and the square root of scan rates complies with the equation,[19, 20] $i_p = 2.99 \times 10^5 n(\alpha n')^{1/2} A C_\infty D_0^{1/2} v^{1/2}$, Where i_p is the peak current, n is the electron-number for the total reaction, n' is the electron-number transferred in the rate-determining step (RDS), α is the electron transfer coefficient of the RDS, A is the electrode surface area, C_∞ is the bulk concentration, D_0 is the diffusion coefficient, v is the potential scan rate. In this paper, the slope of the peak current density *vs.* square root of scan rates is $2.99 \times 10^5 n(\alpha n')^{1/2} A C_\infty D_0^{1/2}$. In the same electrolyte and reaction, the parameters n, C_∞ and D_0 are constant; therefore, the slope is decided by $\alpha n'$. The corresponding slope for Pt@RFC, Pt/RFC and Pt/C-JM is 49.64, 14.76 and 16.16, respectively. It means that the Pt nanoparticles embedded into carbon sphere surface electrode can greatly increase the electron transfer rate in the RDS. Especially for the embedded nanostructure, the electron transfer coefficient increases by about 110% as compared with Pt/RFC electrode.
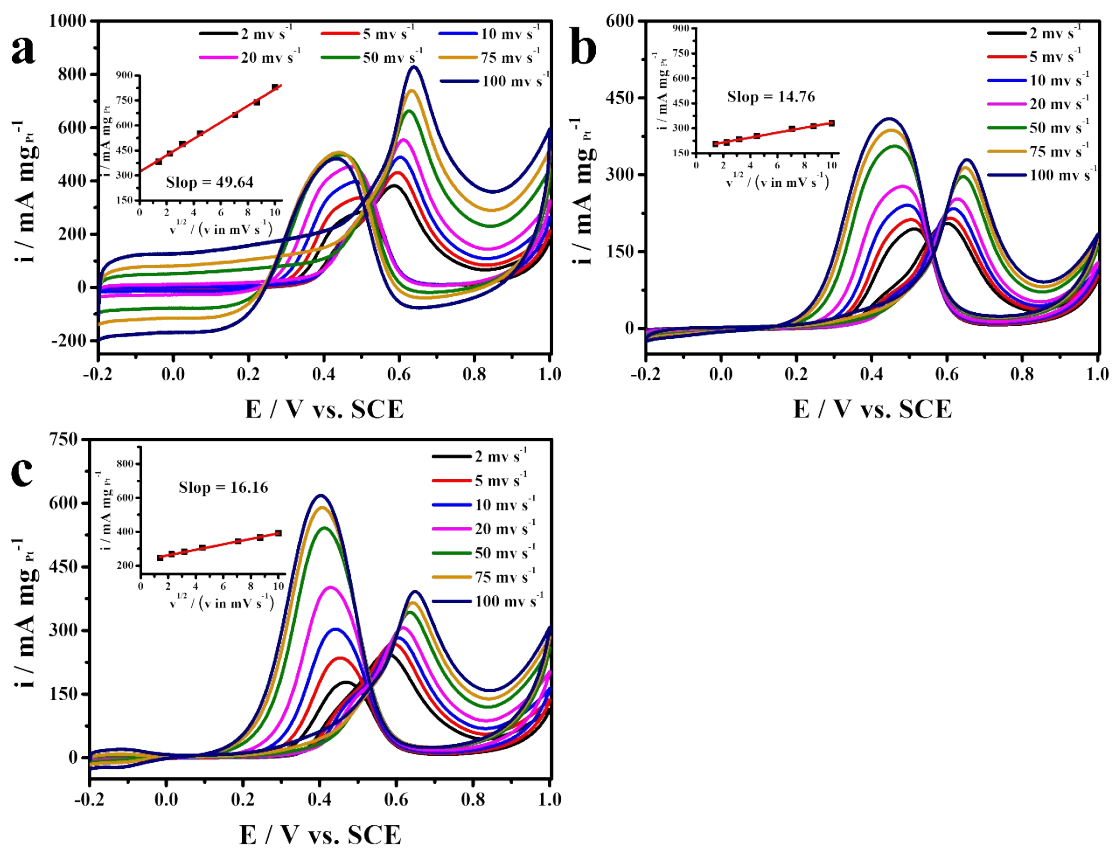
Fig. S8 CVs at the (a) Pt@RFC-8h, (b) Pt/RFC and (c) Pt/C-JM electrodes in 0.5 M H$_2$SO$_4$ solutions containing 1.0 M CH$_3$OH solution with scan rate of 2, 5, 10, 20, 50, 75 and 100 mV s^{-1}.

To further survey the promotional effect of the support for MOR, Tafel slope is calculated on the Pt@RFC, Pt/RFC and Pt/C-JM catalyst at a scan rate of 2 mV s^{-1} and shown in **Fig. 4a**. It is reported that the term 'Tafel slope' in the case of methanol electro-oxidation does not carry its usual fundamental meaning, since straight lines of the electrode potential *vs.* the logarithm of the current density are generally not observed, and that was consistent with our results.[21] It can be seen from **Fig. 4a** that in the linear region from 0 to 0.45 V, the Tafel slope of Pt@RFC electrode is smaller as compared to Pt/RFC and Pt/C-JM modified electrode. Specifically, the Tafel slope of Pt@RFC, Pt/RFC and Pt/C-JM was 91.42, 119.02 and 102.01 mV dec^{-1} respectively, which is consistent with the literature reported slope of 85~195 mV dec^{-1}.[22-25] The lower Tafel slope observed on the Pt@RFC catalyst is also a sign of greater catalytic activity.

As shown in **Fig. S9**, the Nyquist plots for Pt-based catalysts are performed. In agreement with the CV data (as shown in **Fig. 3d**), no methanol oxidation occurred below 0.3 V, so only straight lines are observed in the EIS spectra below 0.3 V. In the range of 0.3~0.4 V, a "pseudo-inductive" behaviour is in observation, which is considered as an ordinary behaviour for methanol electro-oxidation catalyzed by Pt and a sign that methanol is first in dehydrogenation to make the formation of adsorbed CO species oxidatively removed later.[25, 26] As the potential intervals increases to 0.5~0.7 V, the forms of Nyquist plots change drastically. It is indicated the RDS for MOR turns methanol dehydrogenation into CO_{ads} stripping by OH_{ads}.[27] A further increase of potential actually decreases the rate of methanol oxidation, as the adsorption of OH is too strong at high potentials and it starts to inhibit Pt-catalyzed methanol oxidation. This is consistent with the peak potential of ~0.6 V observed by CV. In the EIS spectra, this decrease of reaction rate is reflected in a new 'pseudo-inductive' behavior at >0.8 V. With a further increase of potential beyond 0.8 V, the diameter of the semicircles decreases due to the oxidation of the Pt active sites at high potentials. This is consistent with the current increase at 0.9~1.0 V in the CV. The data from EIS can also be used to compare the activity of various methanol oxidation catalysts. The diameter of the EIS semicircle or arc corresponds to charge transfer resistance, which shows negative correlation with MOR rate.
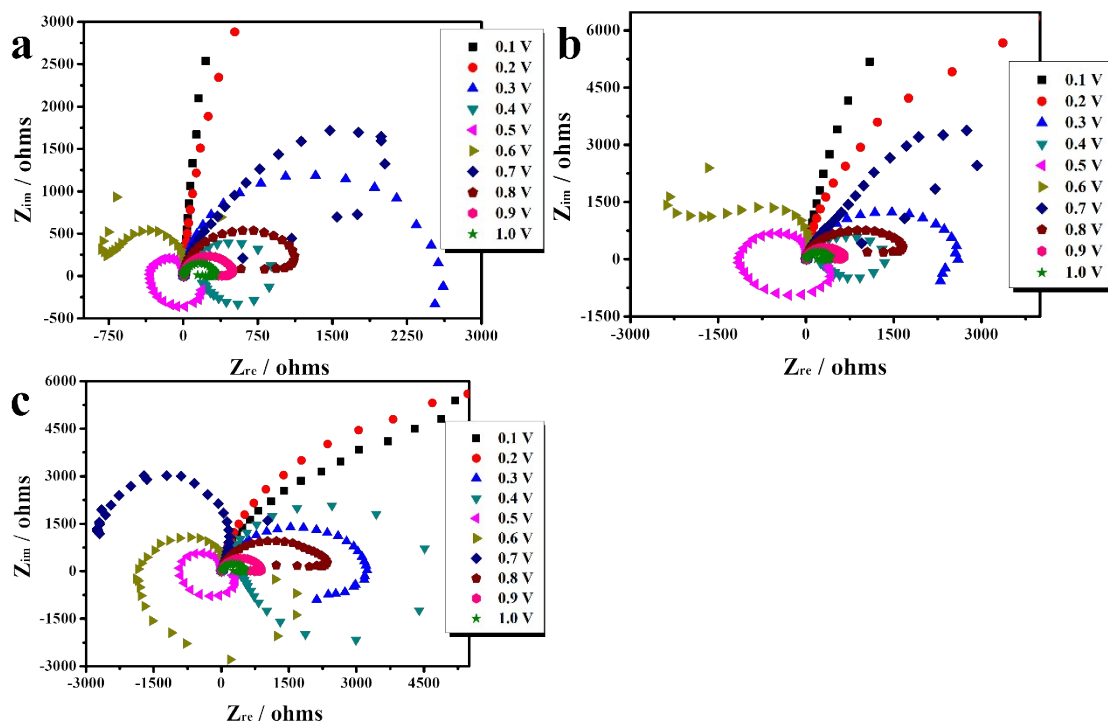
Fig. S9 Nyquist plots of the Pt@RFC-8h, Pt/RFC and Pt/C-JM catalysts in electrochemical methanol oxidation at different potentials (range from 0.1 V to 1.0 V) in 0.5 M H_2SO_4 solutions containing 1.0 M CH_3OH.

Table S8 Fitting results of electrochemical impedance spectroscopy (EIS) for Pt@RFC-8h, Pt/RFC and Pt/C-JM catalysts.

Catalysts	R_S (Ω cm^2)	R_{CT} (Ω cm^2)	CPE (S s^{-n} cm^2)	n (0<n<1)	Iteration	Chi-squared (%)
Pt@RFC-8h	3.205	49.9	3.732E-3	0.9	4	1.048
Pt/RFC	3.054	170.9	5.718E-4	0.894	4	3.073
Pt/C-JM	3.363	144.6	2.996E-3	0.9	4	1.268

In **Fig. S10a-b**, for the Pt@RFC-1h catalyst only 28.27% of the MOR peak current decreases after 3000 cycles, comparing 60.31% of MOR activity decrease to Pt@RFC-20h catalysts. As histograms of the particle sizes distribution shown in **Fig. S10d-e**, the Pt nanoparticles sizes of the Pt@RFC-1h catalyst slightly grown into 5.33 nm, moreover, the initial particle density distributed in the carbon textures is still well-maintained after the durability tests, while the Pt NPs size severely grown from 9.28 nm to 18.83 nm for the Pt@RFC-20h (in **Fig. S10c**). The results indicated that the Pt nanoparticles are more stable in the Pt@RFC during the potential cycling.
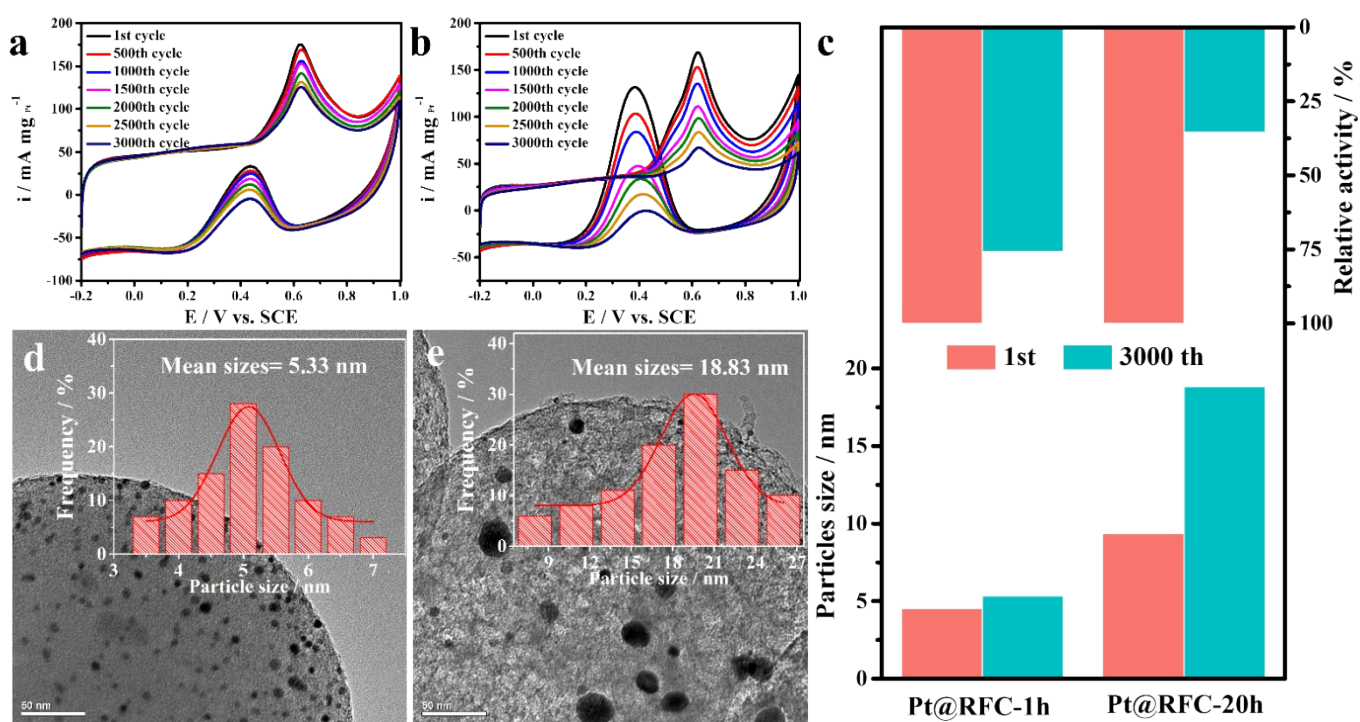

Fig. S10 The comparison mass activity and TEM images with the corresponding particle size distribution histograms of (a, d) Pt@RFC-1h and (b, e) Pt@RFC-20h through ADTs in 0.5 M H_2SO_4 + 1.0 M CH_3OH solutions, respectively. (c) The comparison activity in percent and sizes variation for the two catalysts after ADTs. Scale bar: 50 nm.

Table S9 Comparison of durability and stability through chronoamperometry (CA) measurement and accelerated degradation tests (ADTs) between the novel Pt@RFC-8h catalyst and other Pt-based catalysts reported in the literature

| Sample	Electrolyte	CA			ADTs			Ref.
		Time (s)	Test condition	Decline (%)	Cycles	Test condition	Decline (%)	
Pt@RFC-8h	1.0 M CH$_3$OH + 0.5 M H$_2$SO$_4$	7200	0.5 V *vs.* SCE	13.6	3000	50 mV/s at -0.2~1.0 V	9.01	This work
					10500	50 mV/s at -0.2~1.0 V	35.18	
Pt-RGO/PF-x	1.0 M CH$_3$OH + 0.5 M H$_2$SO$_4$	3600	0.5 V *vs.* SCE	78	500	50 mV/s at -0.2~1.0 V	75	[6]
Pt/CeO$_2$/PANI THNRAs	0.5 M CH$_3$OH + 0.5 M H$_2$SO$_4$	3000	0.65 V *vs.* SCE	~70	~100	65 mV/s at -0.2~1.0 V	2.11	[8]
Pt-Co-P-11.9/CNT,	0.5 M CH$_3$OH + 0.5 M H$_2$SO$_4$	3000	0.7 V *vs.* SCE	80	-	-	-	[9]
Pt/TiO$_2$-C	1.0 M CH$_3$OH + 0.5 M H$_2$SO$_4$	3600	0.5 V *vs.* Ag/AgCl	54	500	50 mV/s at -0.2~1.0 V	16.7	[10]
Pt/Graphene-based	1.0 M CH$_3$OH + 0.5 M H$_2$SO$_4$	600	0.6 V *vs.* SCE	47.5	100	50 mV/s at -0.2~1.0 V	~6	[11]
Pt/TiC NWs	1.0 M CH$_3$OH + 0.1 M H$_2$SO$_4$	100	0.6 V *vs.* SCE	~70	-	-	-	[12]
PtAuP ANTAs	0.5 M CH$_3$OH + 0.5 M H$_2$SO$_4$	5000	0.84 V *vs.* RHE	~70	-	-	-	[28]
Pt$_{10}$Au$_3$Cu$_{44}$	0.5 M CH$_3$OH + 0.1 M HClO$_4$	10000	0.6 V *vs.* RHE	~75	-	-	-	[29]
Ru@Pt$_{0.5}$/C	1.0 M CH$_3$OH + 0.5 M H$_2$SO$_4$	1000	0.75 V *vs.* RHE	~80	1000	200 mV/s at 0~1.2 V	15.9	[30]
Fe$_2$Pt$_1$, C3ISA	0.5 M CH$_3$OH + 0.1 M HClO$_4$	4000	0.45 V *vs.* SCE	71.4	-	-	-	[31]
Pt/SrRuO$_3$ (37.3 nm)	0.5 M CH$_3$OH + 0.1 M H$_2$SO$_4$	3600	0.7 V *vs.* RHE	~33.3	-	-	-	[32]
Pt/TiO$_2$@RFC	1.0 M CH$_3$OH + 0.5 M H$_2$SO$_4$	-	-	-	2000	50 mV/s at -0.2~0.958 V *vs.* SCE	16.14	[33]
Pt@PPy–PANI	0.5 M CH$_3$OH + 0.5 M H$_2$SO$_4$	3600	0.5 V *vs.* Ag/AgCl	72.5	1000	50 mV/s at 0~1.0 V	11.6	[34]
Pt-WP/C	1.0 M CH$_3$OH + 0.5 M H$_2$SO$_4$	3600	0.6 V *vs.* SCE	89.5	1000	50 mV/s at -0.2~1.0 V	37.8	[35]
Pt/PyC$_{60}$	1.0 M CH$_3$OH + 0.5 M H$_2$SO$_4$	1000	0.8 V *vs.* RHE	80	1000	50 mV/s at 0~1.2 V	19	[36]
G-mC-Pt	2.0 M CH$_3$OH + 0.1 M H$_2$SO$_4$	-	-	-	200	100 mV/s at -0~1.0 V *vs.* SCE	~10	[37]
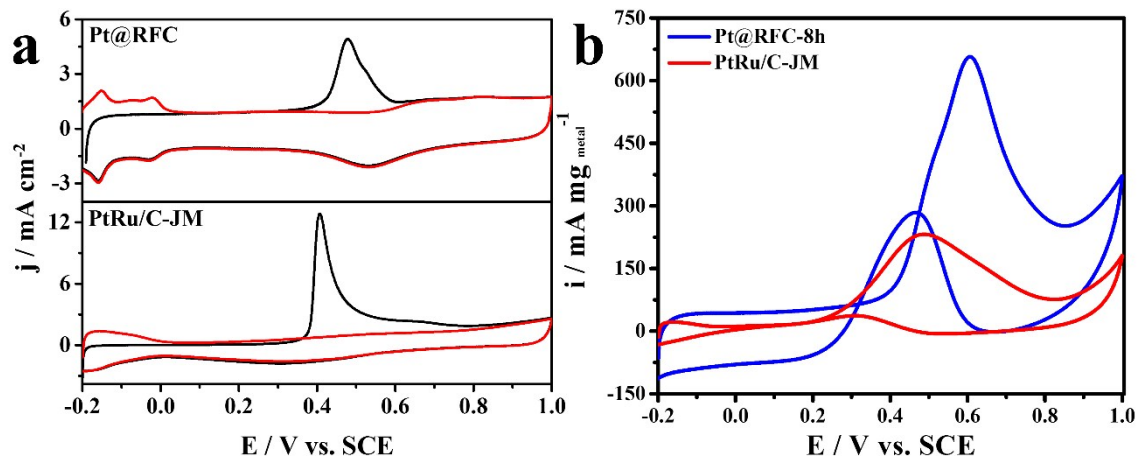
Fig. S11 (a) CO stripping curves of the Pt@RFC-8h and PtRu/C-JM catalysts in 0.5 M H_2SO_4; (b) Mass activity for the comparison catalysts in 0.5 M H_2SO_4 +1.0 M CH_3OH. The scanning rate is 50 mV s^{-1}.
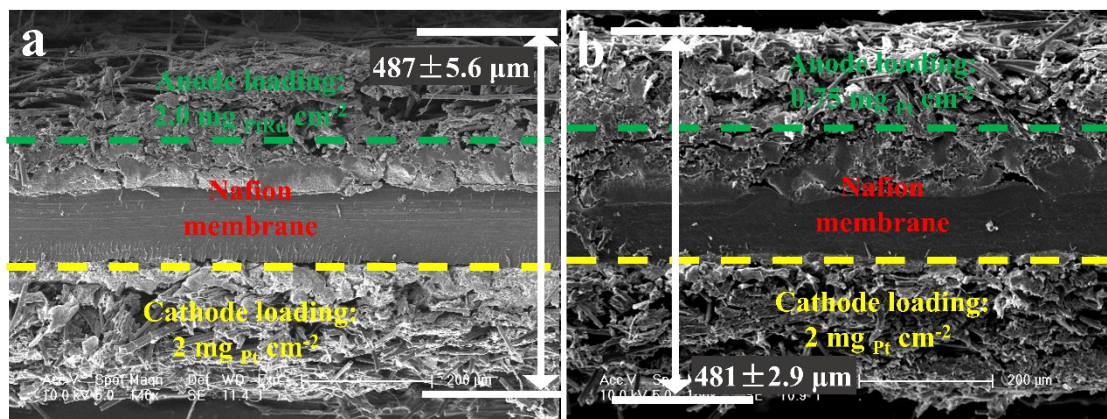
Fig. S12 The structure and composition of the MEA for Pt@RFC (a) and PtRu/C-JM (30% PtRu) (b) catalysts.

As illustrated in **Fig. S13**, fuel cell polarization curve generally exhibits three regions namely activation loss, ohmic loss and mass transport loss,[38] during their operation. The activation region is attributed to the factors such as electrical conductivity, catalytic activity corresponding to the type and amount of catalyst loading, type of electrode.[39, 40] Ohmic region corresponds to the protonic conductivity of the electrolyte i.e. the membrane. Mass-transport region is attributed to factors such as water removal, improved permeability corresponding to porous structure and hydrophobic nature of electrode.[41] Hence the current density plots imply that this special construction with large amounts of macropores generated from spheres packing has played a role in mass-transport region.
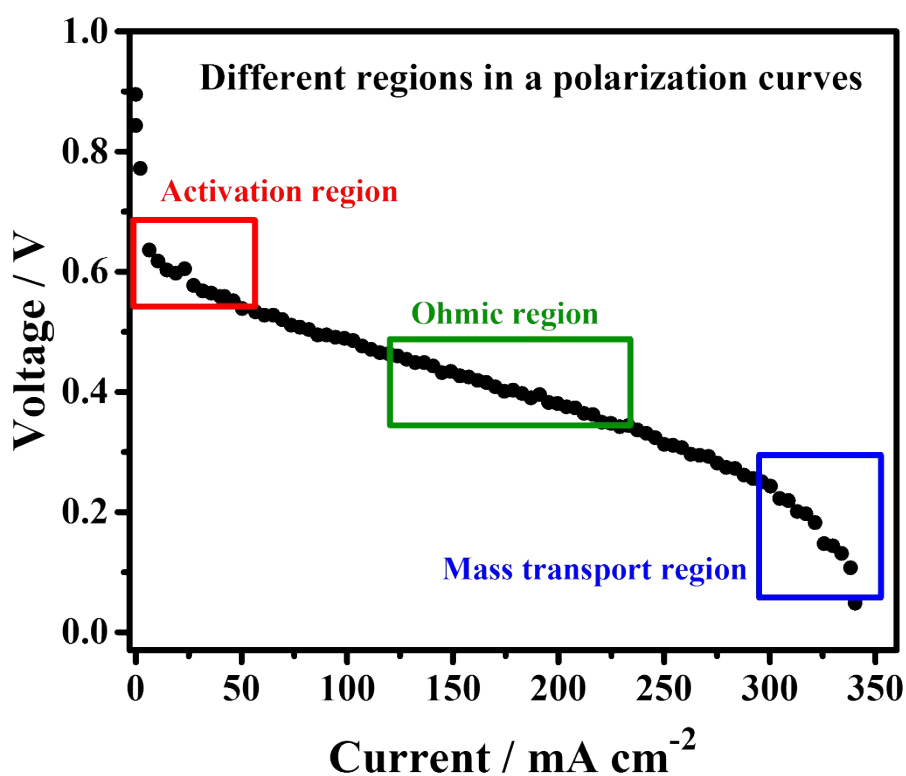

Fig. S13 Illustration of different regions in a general current density plot (fuel cell polarization curve)

References

1. K. Li, J. B. Zhu, M. L. Xiao, X. Zhao, S. K. Yao, C. P. Liu and W. Xing, *ChemCatChem*, 2014, **6**, 3387-3395.
2. X. L. Tang, B. C. Zhang, Y. Li, Y. D. Xu, Q. Xin and W. J. Shen, *Catal Lett*, 2004, **97**, 163-169.
3. V. Selvaraj and M. Alagar, *Electrochem Commun*, 2007, **9**, 1145-1153.
4. F. H. Ribeiro, R. A. D. Betta, G. J. Guskey and M. Boudart, *Chem Mater*, 1991, **3**, 805-812.
5. R. Ganesan and J. S. Lee, *Angew Chem Int Edit*, 2005, **44**, 6557-6560.
6. Q. Xue, J.-K. Li and Z.-Y. Yang, *Langmuir*, 2017, **33**, 872-880.
7. A. A. Siller-Ceniceros, M. E. Sanchez-Castro, D. Morales-Acosta, J. R. Torres-Lubian, E. Martinez and F. J. Rodriguez-Varela, *Appl Catal B-environ*, 2017, **209**, 455-467.
8. H. Xu, A.-L. Wang, Y.-X. Tong and G.-R. Li, *ACS Catalysis*, 2016, **6**, 5198-5206.
9. J. Sun, M. Dou, Z. Zhang, J. Ji and F. Wang, *Electrochim. Acta* 2016, **215**, 447-454.
10. Y.-H. Qin, Y. Li, R.-L. Lv, T.-L. Wang, W.-G. Wang and C.-W. Wang, *J Power Sources*, 2015, **278**, 639-644.
11. L. Zhang, J.-J. Shao, W. Zhang, C. Zhang, X. Zheng, H. Du and Q.-H. Yang, *J. Phys. Chem. C* 2014, **118**, 25918-25923.
12. Z. Qiu, H. Huang, J. Du, X. Tao, Y. Xia, T. Feng, Y. Gan and W. Zhang, *J. Mater. Chem. A*, 2014, **2**, 8003-8008.
13. J. Zhu, M. Xiao, X. Zhao, C. Liu and W. Xing, *J Power Sources*, 2015, **292**, 78-86.
14. M. Xiao, J. Zhu, J. Ge, C. Liu and W. Xing, *J Power Sources*, 2015, **281**, 34-43.
15. W. Wang, Y. Yang, F. Wang, W. Dong, X. Zhou and Z. Lei, *Rsc Advances*, 2015, **5**, 17216-17222.
16. F. Li, H. Gong, Y. Wang, H. Zhang, Y. Wang, S. Liu, S. Wang and C. Sun, *J. Mater. Chem. A*, 2014, **2**, 20154-20163.
17. X. Wang, W. Wu, X. Xiang and W. Li, *J Power Sources*, 2014, **259**, 255-261.
18. Y. Xiao, Z. Fu, G. Zhan, Z. Pan, C. Xiao, S. Wu, C. Chen, G. Hu and Z. Wei, *J Power Sources*, 2015, **273**, 33-40.
19. L. Feng, Q. Lv, X. Sun, S. Yao, C. Liu and W. Xing, *J Electroanal Chem*, 2012, **664**, 14-19.
20. Y. Wang, X. Wu, B. Wu and Y. Gao, *J Power Sources*, 2009, **189**, 1020-1022.
21. S. L. Gojković, T. R. Vidaković and D. R. Đurović, *Electrochim. Acta* 2003, **48**, 3607-3614.
22. M. Yin, Y. Huang, Q. Li, J. O. Jensen, L. N. Cleemann, W. Zhang, N. J. Bjerrum and W. Xing, *ChemElectroChem*, 2014, **1**, 448-454.
23. W. Xu, T. Lu, C. Liu and W. Xing, *J. Phys. Chem. B* 2005, **109**, 7872-7877.
24. C. Z. He, H. R. Kunz and J. M. Fenton, *J Electrochem Soc*, 1997, **144**, 970-979.
25. G. Wu, L. Li and B. Q. Xu, *Electrochim. Acta* 2004, **50**, 1-10.
26. É. C. G. Rufino and P. Olivi, *Int. J. Hydrogen. Energ.*, 2010, **35**, 13298-13308.
27. J. Chang, L. Feng, C. Liu, W. Xing and X. Hu, *Energy Environ. Sci. *, 2014, **7**, 1628-1632.
28. L. Zhang, L.-X. Ding, H. Chen, D. Li, S. Wang and H. Wang, *Small*, 2017, **13**.
29. X. Wang, L. Zhang, H. Gong, Y. Zhu, H. Zhao and Y. Fu, *Electrochim. Acta* 2016, **212**, 277-285.
30. J. Xie, Q. Zhang, L. Gu, S. Xu, P. Wang, J. Liu, Y. Ding, Y. F. Yao, C. Nan, M. Zhao, Y. You and Z. Zou, *Nano Energy*, 2016, **21**, 247-257.
31. J. Wang, Z. Wang, S. Li, R. Wang and Y. Song, *Nanoscale*, 2017, **9**, 4066-4075.
32. M. E. Scofield, C. Koenigsmann, D. Bobb-Semple, J. Tao, X. Tong, L. Wang, C. S. Lewis, M. B.

Vukmirovic, Y. Zhu, R. R. Adzic and S. S. Wong, *Catalysis Science & Technology*, 2016, **6**, 2435-2450.

33. K. Li, M. Xiao, Z. Jin, J. Zhu, J. Ge, C. Liu and W. Xing, *Electrochim. Acta* 2017, **235**, 508-518.
34. O. Karatepe, Y. Yildiz, H. Pamuk, S. Eris, Z. Dasdelen and F. Sen, *RSC Advances*, 2016, **6**, 50851-50857.
35. Y. Duan, Y. Sun, S. Pan, Y. Dai, L. Hao and J. Zou, *ACS Appl. Mat. Interfaces* 2016, **8**, 33572-33582.
36. X. Zhang and L.-X. Ma, *J Power Sources*, 2015, **286**, 400-405.
37. L. Nan, W. Yue and Y. Jiang, *J. Mater. Chem. A*, 2015, **3**, 22170-22175.
38. S. C. Thomas, X. M. Ren, S. Gottesfeld and P. Zelenay, *Electrochim. Acta* 2002, **47**, 3741-3748.
39. C. Eickes, P. Piela, J. Davey and P. Zelenay, *J Electrochem Soc*, 2006, **153**, A171-A178.
40. P. Piela, R. Fields and P. Zelenay, *J Electrochem Soc*, 2006, **153**, A1902-A1913.
41. S. Uhm, S. T. Chung and J. Lee, *J Power Sources*, 2008, **178**, 34-43.